

1
2
3
4
5
6
7 An Experimental and Modeling Study of CaCO₃ Nucleation and Inhibition Under a Dynamic
8 Oversaturation Regime with Implications for Energy Production from Subsurface Reservoirs
9

10
11
12
13
14
15
16
17 Authors: Amit G Reiss^{1*}, Xin Wang¹, Yuqing Ye¹, Amy T Kan¹, and Mason B Tomson¹

18 * Corresponding author: reissam@post.bgu.ac.il
19

20 Affiliations
21

22 1- Rice University, Department of Civil and Environmental Engineering, 6100 Main street,
23 Houston, TX, USA. 77005.
24
25
26
27
28
29
30
31
32
33
34
35
36
37
38
39
40

Abstract

Energy production from subsurface reservoirs perturbs the equilibrium between fluids and the surrounding rocks. As the saturation increases, nucleation begins, forming a scale that is detrimental to production. Inhibitor addition for scale prevention is a common practice with significant economic and environmental costs. Traditional experiments to determine induction times (t_{ind}) and evaluate inhibitor efficiency are performed under constant oversaturation. Similarly, constant oversaturation is used in both the empirical and the classical nucleation theory modeling schemes used for scale prediction. Subsequently, experiments and models do not address the dynamic nature of oversaturation increase during energy production.

We developed an experimental system for quantitative investigation of nucleation kinetics under a regime of dynamic oversaturation and a simple algorithm for determining t_{ind} from laser measurements. Using our system, we studied the precipitation kinetics of CaCO_3 minerals at a pH of ~ 6.76 , ionic strength of $I = 1\text{m}$, temperature range of $50\text{--}90^\circ\text{C}$, and varying rates of oversaturation increase. We quantified the effect of a potent inhibitor (Polyamino Polyether Methylene Phosphonate; PAPEMP) on the t_{ind} and the forming solid phase. Finally, we developed a numerical model that explicitly accounts for the dynamic nature of oversaturation.

Here, we present our experimental system, results, and modeling scheme. We show that for a given set of conditions, calcite induction occurs at a similar oversaturation, regardless of the rate at which oversaturation increases. Moreover, we show that PAPEMP retards CaCO_3 nucleation at below ppm levels and that it has a temperature-dependent effect on polymorphism. Lastly, we suggest that expanding existing models such that:

$$t_{ind} = f(\Delta SI) * f(static)$$

Where $f(\Delta SI)$ is a function of oversaturation with time and $f(static)$ are existing modeling schemes, adequately describe the dynamic nature of oversaturation and show a form of $f(\Delta SI)$ that provides an excellent fit with measured t_{ind} .

Keywords: CaCO_3 induction time, calcite induction time, metastability zone, Polyamino Polyether Methylene Phosphonate (PAPEMP), Nucleation kinetics, scale inhibition

1. Introduction

Subsurface brines and fluids become supersaturated and precipitate minerals during energy production from hydrocarbon and hydrothermal reservoirs. The precipitation of these minerals causes scale formation that is detrimental to production. Scaling clogs pipes, damages machinery, and reduces the porosity and permeability of reservoir rocks (Kamal et al., 2018; Regenspurg et al., 2015). Carbonate and sulfate minerals are the most common scale-forming minerals, with calcite being the most abundant.

Adding scale inhibitors to prevent precipitation is a routine practice during energy production. Typical scale inhibitors are organic molecules with either phosphonate, sulfonate, or carboxylate functional groups. The addition of these chemicals, even at ppm levels and below, retards precipitation (Reiss et al., 2020), alters crystal habit (Reiss et al., 2020; Weber et al., 2016), and changes the mineral phase by stabilizing less-stable polymorphs (Gopi et al., 2013; Gopi and Subramanian, 2012; Sanjiv Raj et al., 2021). Subsequently, much effort has been directed towards determining inhibitor impact on kinetics, habit, and polymorph selection.

Traditionally, the interplay between inhibitors and nucleation kinetics is studied under static setups where the initial conditions of the fluid phase are constant until crystal nucleation and growth alter the chemistry. However, during energy production from geological reservoirs, the saturation with respect to scale-forming minerals changes due to several possible processes such as degassing and changes in pH, temperature changes, evaporation, mixing of brines, etc. Subsequently, contrary to static experimental setups, scale formation during energy production occurs under increasing saturation.

Filed observations show that fluids being concentrated and becoming oversaturated can remain metastable towards several mineral phases for extended durations before an oversaturation threshold is passed and nucleation begins (Rosenberg et al., 2018). The width of the ‘metastable zone’ (i.e., the difference between equilibrium and oversaturation at which nucleation occurs), is key for controlling industrial crystallization and the impact the rate of oversaturation increases due to various temperature gradients in crystallizers is extensively studied (Duroudier, 2016). It was found that for low-temperature gradients, the width of the metastable zone for highly soluble salts (e.g., KCl and NaCl) depends on the temperature gradient (up to several °C/h) (Nývlt, 1968). However, under temperature gradients that are typical of energy production and beyond (e.g., ≥ 0.5 °C/min), the width of the metastable zone is insensitive to the gradient and $\rightarrow 0$ (i.e., crystal formation is immediate) (Navarathna et al., 2023).

The impact of the saturation increase rate on the width of the metastability zone for gypsum, barite, and some carbonate phases (witherite, strontianite) where previously determined for diffusion-controlled systems at ambient temperatures (Prieto et al., 1994). These experiments found a dependency between the rate of saturation increase and the oversaturation at which the nucleation occurs. However, due to the slow rate of diffusion and subsequent long induction times (weeks to months) compared to the duration of fluid transport and induction during energy production (typically up to a couple of hours) these results are not directly applicable to energy production scenarios.

Identifying the oversaturation at which nucleation will occur during energy production will provide an improved assessment of scaling risk and be utilized for adjusting mitigation strategies. However, to date, the impact of the rate of the saturation increase on the nucleation kinetics and the values of oversaturation at which nucleation occurs have not been determined for major scale-forming minerals under conditions that are relevant for energy production. More importantly, current models of nucleation kinetics and induction time prediction for these conditions are derived and validated from static experiments (see discussion in section 4.4.1). Quantitatively determining the impact of dynamic saturation on the nucleation kinetics under relevant conditions for the major scale-forming minerals and developing modeling schemes to represent these effects will be a step forward for scale prediction and control.

Contrary to the kinetics, inhibitor impact on polymorphism and crystal habit is often derived from dynamic systems where SI is gradually increased by titrations, fluid injection, degassing, or applying a temperature gradient (Gopi et al., 2013; Gopi and Subramanian, 2012; Nicoleau et al., 2019; Sanjiv Raj et al., 2021). Subsequently, the information on nucleation kinetics, crystal habit, and polymorph selection are often obtained under different conditions.

The goal of this research was to study CaCO_3 nucleation and inhibition under increasing saturation. Specifically, we aimed to 1. Develop a simple apparatus and workflow that will enable: a) a quantitative study of CaCO_3 precipitation at the slightly acidic to acidic conditions prevailing in many subsurface reservoirs from which hydrocarbons (Dai et al., 2022a) or hydrothermal fluids (Utami et al., 2014) are produced; b. allow for a simple, accurate, determination of nucleation kinetics with high reproducibility; and c) determine the CaCO_3 polymorph alongside the kinetics. 2. Derive a quantitative model for predicting induction times under increasing SI under conditions that are relevant to energy production.

2. Methodology

2.1 Brine preparation

Brines for the experiments were made with analytical grade $\text{CaCl}_2 \cdot 2\text{H}_2\text{O}$ (Sigma-Aldrich), NaCl (Sigma-Aldrich), NaHCO_3 (Fischer Chemical), 1N HCl (Fischer Chemical), and Double deionized water (DDW; resistivity of 18 ohm/cm). The inhibitor used is a commercially available product with 48-52% Polyamino Polyether Methylene Phosphonic Acid (PAPEMP) active ingredient. Three brines were used in each experiment, cationic brine, anionic brine, and reaction cell brine. The reaction cell brine was a 1 m NaCl solution. The anionic brine contained 0.12 m NaHCO_3 with NaCl to adjust the ionic strength to 1 m. The cationic brine contained 0.24 m CaCl_2 with NaCl to adjust the ionic strength to 1 m. HCl was added to the cationic brine to maintain the pH during the duration in which the mixed brine in the reaction cell is oversaturated during the experiments within ± 0.03 units. The amount of acid to add was calculated with Rice Universities ScaleSoftPitzer (SSP) software package (see thermodynamic calculations section 2.3).

In the inhibitor-containing experiments, PAPEMP was added to the reaction cell and anionic brines. The concentration of the inhibitor in the anionic brine was double the concentration

in the reaction cell so that when the anionic and cationic brines were injected into the reaction cell (see experimental setup section 2.2) the inhibitor concentration remained constant.

2.2 Experimental setup

Figure 1 depicts the experimental system. The reaction cell is a customized ACE heavy-walled glass tub with a PTFE cap. Three holes were drilled through the cap to enable tubing for the inflow of the ionic brines and effluent outflow. The framework of the experimental system is a GC oven that was placed above a magnetic stirrer. The magnets on the stirrer were replaced by strong rare earth magnets enabling stirring fluids in the reaction cell inside of the oven. Two holes were drilled into the oven opposite each other. The reaction cell was fixed between the two drillings with an apparatus specifically designed for this purpose. A green laser source and a photodiode were situated on opposite sides of the oven, near the two drillings, so that the laser beam traveling between the source and photodiode passed through the reaction cell. The photodiode was connected to a signal amplifier and a data logger was used for recording the laser intensity at intervals of one second. An additional inlet, drilled in the side of the oven, was used for connecting the reaction cell and the ionic reservoirs situated outside the oven. The cationic and anionic reservoirs were 50 ml plastic syringes. These syringes were placed on top of a KD programmable double syringe pump. The effluent flowed out of the reaction cell via an additional tube connected through an opening at the top of the oven. To prevent degassing and CO₂ escape, the effluent tube was connected to a 20 PSI backpressure regulator.

We conducted experiments with a mass exchange rate, k_w , ($k_w = Q/V_{\text{cell}}$) of 0.53 at 50, 70, and 90 °C. Plots of SI in time for all mass exchange rates and temperatures are presented in supplementary 1 datafile. At each temperature we performed experiments with 0, 0.25, 0.5, and 0.7 ppm PAPEMP. In addition, to test the effect of the rate at which SI changes, we performed experiments at 90 °C (0 and 0.5 ppm inhibitor) under three additional flow rates that produced mass transfer coefficients of 0.38, 0.8, and 1.15. The pH during the 50 °C and 70 °C experiments was 6.78 and 6.76 for the 90 °C experiments. We performed at least three experiments under each combination of T, mass transfer coefficient, and inhibitor concentration. For A total of 79 experiments

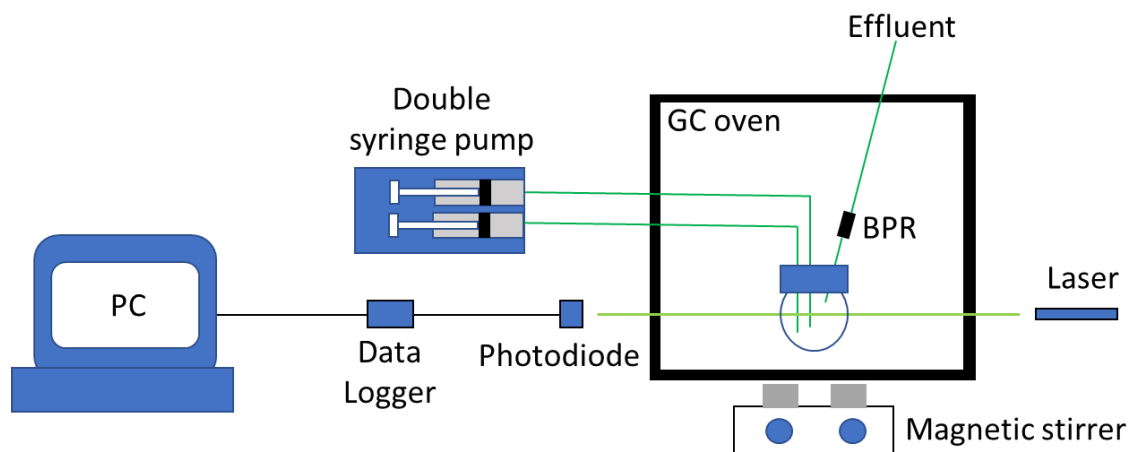


Figure 1. The experimental setup.

The end of each experiment was determined by a change in laser intensity. At the end of each experiment, the crystals were separated from the solution by filtration using 0.45 µm dark filter Wautman paper. XRD (Rigaku D/Max ultima II powder XRD and PDXL database) and SEM (FEI Quanta 400 ESEM) were used to determine the precipitating polymorph and imaging the crystals.

2.3 Thermodynamic calculations

The Pitzer model was used to calculate the amount of acid inflow to maintain pH, and the saturation index (SI, equation 1) throughout the experiment. Pitzer's model is incorporated into several software packages (e.g., PHREEQC, Geochemist Workbench, etc), however, calculated SI varies between them and it is necessary to select a software package and thermodynamic database that was verified to fit the experimental conditions (Reiss et al., 2021). Here, we used the Rice SSP software package. SSP is specifically designed for calculating the thermodynamic properties of brines at elevated temperatures and was verified to be accurate for CaCO₃ polymorphs under the conditions of our experiments (Dai et al., 2017).

$$SI = \log \left(\frac{IAP}{K_{sp}} \right) = \log \left(\frac{a_{Ca^{2+}} * a_{CO_3^{2-}}}{(a_{Ca^{2+}} * a_{CO_3^{2-}})_{eq}} \right) \quad (1)$$

IAP is the ion activity product, *K_{sp}* is the solubility product, and *a_i* is the activity of the *i*th species.

3. Results

The recorded measured laser intensity over the duration of all experiments are attached as supplementary S2.

4. Discussion

4.1 A simple algorithm for determining *t_{ind}* from laser measurements

The induction time (*t_{ind}*) is defined as the time laps between the creation of supersaturation (i.e., SI > 0) and the appearance of the nucleating phase. The ability to identify the appearance of crystals is method specific and *t_{ind}* for a given system varies with techniques. Using the interference to light travelling through a reaction cell following crystal formation is a simple way for continuously monitoring for mineralization. Due to its simplicity, compatibility with any transparent reactor, and easy application under a wide range of environmental conditions, using laser intensity as done here is extremely useful for studying the nucleation kinetics of scale-forming minerals. However, fluctuations in laser intensity is a challenge causing researchers to limit the use of this technique to experiments with short induction times (Westin and Rasmuson, 2005). To overcome this challenge, we fitted the measured laser intensity curve with a sigmoidal/logistic function (equation 2):

$$\text{Laser intensity}_{(t)} = \frac{a-b}{1+(\frac{t}{c})^p} + b \quad (2)$$

where a is the laser intensity before induction time, b is the lowest laser intensity value following induction, t is time, c is the midpoint of the slope of the curve linking a and b , p is the curvature (angle) between the pre-nucleation value of the laser and the downward sloping line immediately after t_{ind} .

The fitting procedure produces a calculated laser intensity curve that is not affected by the fluctuations in the laser source (Figure 2).

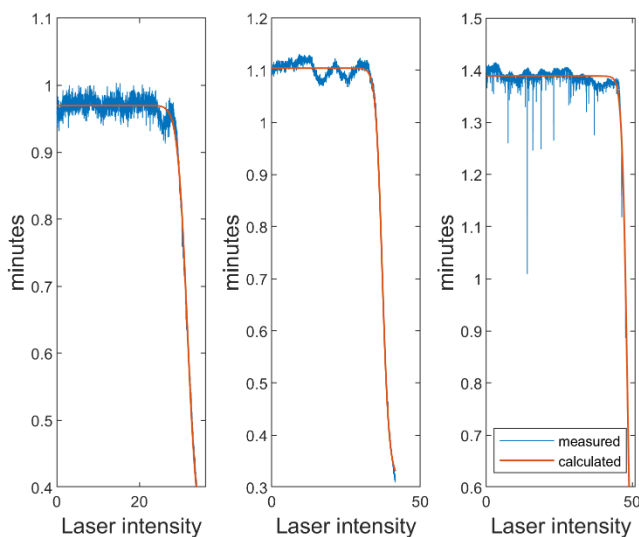


Figure 2. The measured VS. calculated laser intensity. The induction time is derived from the calculated laser values that smooth out laser instability.

The induction time is the time where the intensity VS. time curve sufficiently shifts from the pre-nucleation plateau. Mathematically, this is derived by inserting the c and p fitting parameters from equation 2 into equation 3:

$$t_{ind}^{sufficient\ shift} = c * criterion^{1/p} \quad (3)$$

The criterion in equation 3 is a value that depends on the definition of sufficient shift from the pre-nucleation plateau. It was recently suggested, based on the Mie light theory, that a 1% change in laser intensity is sufficient to determine induction (Dai et al., 2019). Under such a circumstance, the criterion would be 1/99 and equation 3 becomes:

$$t_{ind}^{for a 1\% drop} = c * \left(\frac{1}{99}\right)^{1/p} \quad (4)$$

Equation 4 is a robust mathematical form that overcomes the pre-nucleation fluctuations in laser intensity and allows for a simple objective determination of t_{ind} in long experiments. A full description of the algorithm we used is presented in appendix A.

4.2 Evaluating the experimental system

The average induction time and SI at induction for all the experimental conditions are provided in Table 1. Comparing the induction times for the different temperatures, inhibitor concentrations, and mass transfer rates shows that: the induction time at a given temperature and mass transfer rate increases with inhibitor concentration, an inverse relationship exists between temperature and induction time for all inhibitor concentrations (Figure 3a), and that the induction time is shortened by faster increase in SI (Figure 3b). These trends agree with the general understanding of the role the environmental parameters play in nucleation kinetics and serve as an initial qualitative test of the system's operation and the experimental results.

We performed a quotient rejection test, and contrary to the measured induction times that vary widely with the rate of mass transfer, the SI at induction is similar at a 90% confidence level for the different mass exchange rates (Figure 3c) indicating that the width of the metastable zone is impervious to the oversaturation increase rate under the current experimental conditions. Recently, similar behavior was reported for halite nucleation in a cooling system (without inhibitors) where the induction time had an inverse relationship with the rate of cooling but the SI value at induction was independent of the cooling rate (Navarathna et al., 2023). Such observations are key for modeling nucleation kinetics in dynamic systems and are further discussed in section 4.4.2.

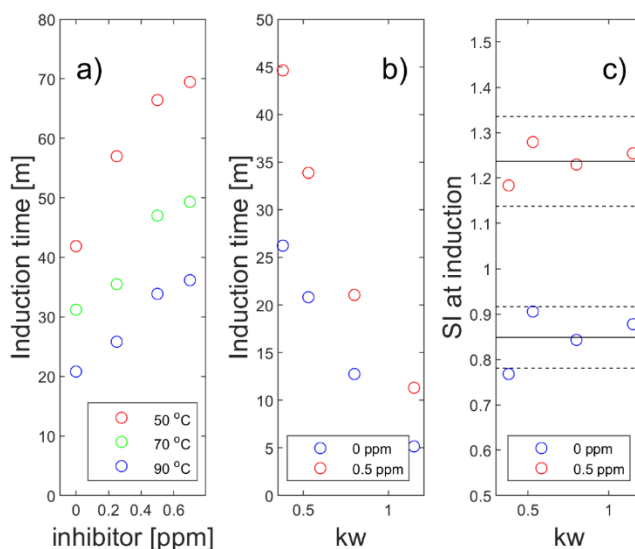


Figure 3. a) The average induction time as a function of inhibitor concentration at 50, 70, and 90 °C. b) The average induction time at 90 °C as a function of the rate of mass transfer with no

inhibitor and 0.5 ppm inhibitor. c) The SI at induction for the different values of kw with 0 and 0.5 ppm inhibitor. The solid lines are the average SI at induction and the dashed lines are $\pm 8\%$ of the average, similar to the larger RSD on SI (table 1). A quotient rejection test shows that for a given concentration of inhibitor and a 90% confidence, the SI is similar for all values of kw.

Quantitatively, the relative standard deviation (RSD) on the induction time and on the SI is better than 10% and compare with RSD values reported from static experimental systems (Rabizadeh, 2023). These results demonstrate that dynamic experimental setups, that better represent actual conditions of scale formation, can be adopted without increasing the uncertainty of the measured induction time. Consequently, the experimental design described above can be adopted for studying nucleation under dynamic conditions and enables a simultaneous determination of the kinetics, crystal habit, and polymorphism in a single experiment.

Table 1 - Summary of experiments

T (°C)	kw (Q/V) (time ⁻¹)	[inhibitor] (ppm)	# of experiments	Tind (minutes)	RSD (T _{ind})	SI	RSD (SI)
90	0.38	0	5	26.2	6%	0.77	6%
90	0.53	0	7	20.8	9%	0.91	8%
90	0.80	0	6	12.8	3%	0.84	3%
90	1.15	0	4	10.0	3%	0.88	3%
90	0.53	0.25	7	25.8	5%	1.07	3%
90	0.38	0.5	4	44.6	2%	1.18	1%
90	0.53	0.5	3	33.9	1%	1.28	1%
90	0.80	0.5	3	21.1	2%	1.23	1%
90	1.15	0.5	4	16.3	3%	1.25	2%
90	0.53	0.7	3	36.2	1%	1.33	1%
70	0.53	0	3	31.2	1%	1.10	1%
70	0.53	0.25	3	35.5	7%	1.19	5%
70	0.53	0.5	6	46.2	4%	1.38	2%
70	0.53	0.7	4	49.3	3%	1.43	1%
50	0.53	0	8	41.9	5%	1.16	3%
50	0.53	0.25	3	57.0	6%	1.37	3%
50	0.53	0.5	3	66.4	4%	1.47	2%
50	0.53	0.7	3	69.5	3%	1.50	1%

4.3 PAPEMP and CaCO₃ Polymorphism

CaCO₃ has three naturally occurring polymorphs with distinct morphology: rhombohedral calcite, orthorhombic aragonite, and hexagonal vaterite. Crystal polymorphism, habit, and size distribution determine the ability of the forming solid to adhere to surfaces, clog pipes, and damage machinery and are therefore especially important in scaling processes. Generally, elongated crystal habits are more prone to be detrimental to production (Glade et al., 2010; Mi & Elimelech, 2010). Due to its importance, previous studies aimed to determine the impact different inhibitors have on CaCO₃ polymorphism and crystal habit (Didymus et al., 1993; Gopi et al., 2013; Gopi and Subramanian, 2012; Sanjiv Raj et al., 2021; Tang et al., 2008; Wang et al., 2005; Weber et al., 2016). However, although PAPEMP has a high tolerance for calcium, is

effective at inhibiting both calcium carbonates and sulfates, is effective at both high and low pH (Gill, 1999; Tang et al., 2008), and is the inhibitor of choice in major energy production companies (personal communications with flow assurance engineers), very little research has been done to determine this inhibitor's effects on precipitation kinetics and polymorph selection.

The only previous work (to our knowledge) that specifically tested PAPEMP, found that at 60 °C (and unconstrained pH) this inhibitor does not affect the formed mineral assemblage (Tang et al., 2008). In our study, where the pH, temperature, $\text{Ca}^{2+}/\text{HCO}_3^-$, and ionic strength are held constant until induction, only calcite was detected in the solutions with no inhibitor. The addition of PAPEMP in concentrations of 0.25-0.7 ppm did not change the mineral assemblage at 70 °C and 90 °C. However, at 50 °C, with PAPEMP, a mixture of vaterite and calcite precipitated regardless of inhibitor concentration (Figure 4). Previous studies observed that the addition of inhibitors will alter the CaCO_3 mineral assemblage at some temperatures while not affecting polymorphism at another temperature (Gopi et al., 2013; Gopi and Subramanian, 2012). However, their experimental protocol consisted of gradually adding a bicarbonate solution to a calcium solution so the pH and $\text{Ca}^{2+}/\text{HCO}_3^-$ ratio, both key for CaCO_3 precipitation, were not constrained. Subsequently, the addition of inhibitors might not be the only cause for the observed change in polymorphs. The experimental system used in this study enables isolating the effect of the inhibitor by maintaining a constant pH and $\text{Ca}^{2+}/\text{HCO}_3^-$ ratio. Therefore, our results unequivocally demonstrate that the impact of PAPEMP on CaCO_3 polymorph selection is temperature dependent.

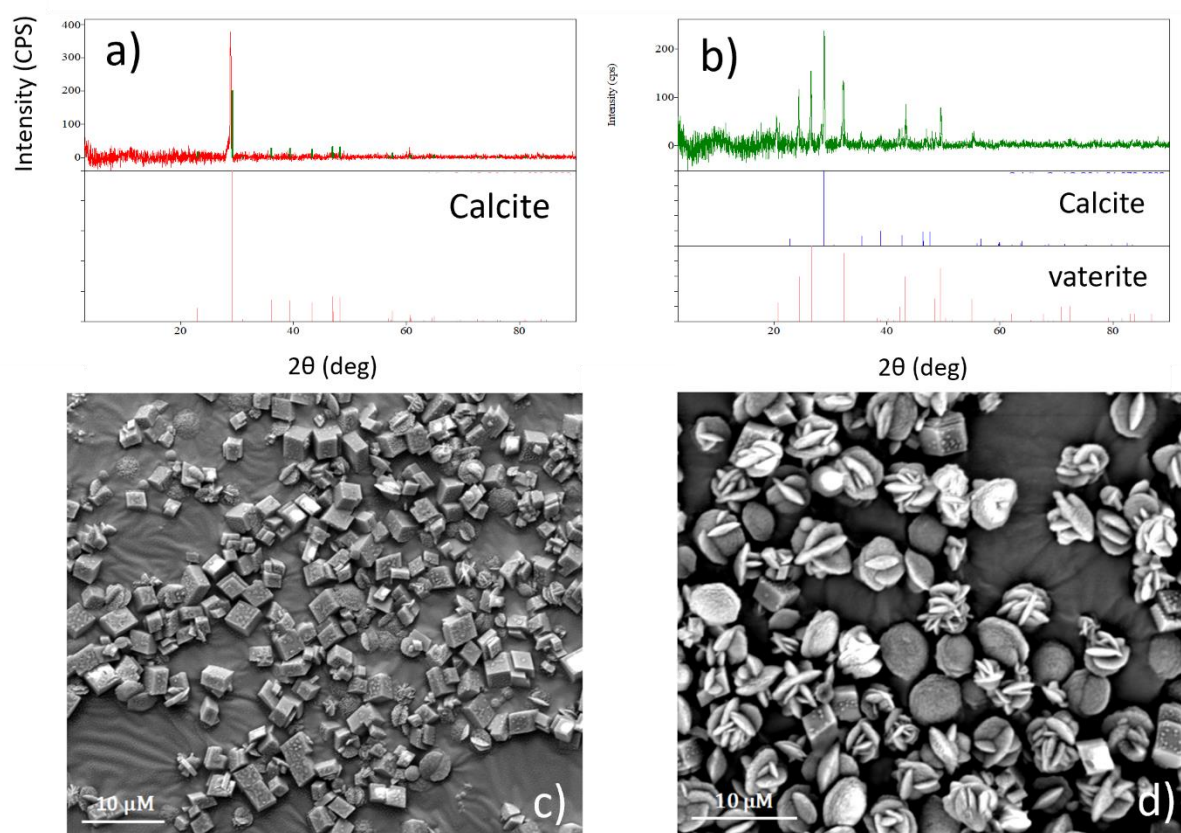


Figure 4. XRD analysis and SEM images of the precipitated solids showing that at 50 °C with no inhibitor (a) calcite is the precipitated solid and that with added PAPEMP (0.25 ppm) a mixture of calcite and vaterite precipitate (b). c) calcite crystal precipitated at 50 °C without inhibitor showing mostly rhombohedral habit, and d) the calcite and vaterite crystals precipitated at 50 °C in the presence of PAPEMP. Notice a combination of crystal habits. XRD and SEM images of other temperatures are added in supplementary 1.

Observations of the pathway taken by dissolved Ca^{2+} and HCO_3^- ions to become calcite suggest that this is a stepwise process starting with the formation of an amorphous calcium carbonate (ACC) phase. The ACC then develops into vaterite that later transform to calcite via a dissolution reprecipitation process (Rodriguez-Blanco et al., 2011). To date, the impact common inhibitors have on this pathway are unknown. From our results we cannot conclude if at 50 °C PAPEMP impedes the transformation of vaterite into calcite, or alternatively, that without inhibitor calcite is the first phase to form and the addition of PAPEMP at 50 °C prevents its formation and/or facilitates the nucleation of vaterite. However, whatever the mechanism is, our results show that the effect of PAPEMP on CaCO_3 are temperature dependent.

4.4 Towards modeling scale formation under dynamic conditions

4.4.1 Models for nucleation kinetics – the current state

Models of nucleation kinetics that can predict the induction time are useful for many processes in natural environments, for interpreting mechanisms of geological and hydrogeological brine development, and for engineering applications. Due to the wide importance of nucleation kinetics, many studies have used induction times, derived from static experiments, to model the nucleation kinetics under a wide range of conditions. The two common approaches taken to model the kinetics are by using the framework of the classical nucleation theory (CNT), or by using a set of empirical equations. According to the CNT, the rate of nucleation (J_s) of a mineral depends on the temperature, saturation state, and the interfacial tension, and is given by:

$$J_s = A \exp \left(- \frac{\beta V_m^2 \sigma^3 N_A f(\theta)}{(RT)^3 \ln^2 \Omega} \right) \quad (5)$$

Where A is a pre-exponential factor, β is a shape factor, σ is the interfacial tension between the solution and the forming crystal, V_m is the molar volume of the forming crystals, N_A is Avogadro's number, $f(\theta)$ is a correction factor for heterogenous nucleation, R and T are the gas constant and temperature and Ω is the saturation ratio.

In recent years, a growing number of experimental observations suggest that nucleation of the common scale-forming minerals does not follow the classical path (for a discussion of classical VS. non-classical nucleation the reader is referred to a recent textbook (Van Driessche et al., 2017)). Whether calcite nucleation proceeds via a classical pathway is still being debated

(Smeets et al., 2017). However, while the theoretical validity of the classical theory to the nucleation of calcite is still under debate, it is generally agreed that equation 5 provides a robust mathematical framework for modeling nucleation whether the process is classical or not, and this equation has been successfully incorporated into kinetic nucleation models (Dai et al., 2022b, 2019; Peters et al., 2024; Rendel et al., 2018; Reznik et al., 2012).

Although mathematically equation 5 can provide good agreement with experimental observations it is often counter-productive for interpreting the impact of scale inhibitors. First, literary values of the interfacial tension term (σ) for common scale-forming minerals span over an order of magnitude or more (Dai et al., 2019; Reiss et al., 2021). This variety enables an empirical selection of a value that fits the specific observations. More importantly, at the low concentrations at which inhibitors are added (typically from below up to several ppm), the complexation of lattice-building ions by inhibitors does not alter the saturation. Subsequently, based on the CNT, inhibitor influence on the nucleation kinetics is often interpreted as being a result of an increase in the interfacial energy (Curcio et al., 2010; Hasson et al., 2003; Van Der Leeden et al., 1993; Vasina et al., 1996). However, as recently stated elsewhere, thermodynamic considerations and measurements of contact angle between inhibitor-containing fluids and mineral surfaces suggest the opposite (Nicoleau et al., 2019).

An alternative approach to model nucleation kinetics and the impact of inhibitors would be to use empirical equations that do not pre-suppose a mechanism of nucleation and that are independent of parameters, such as the interfacial tension term, that their values are uncertain and their literary values widely vary. He et al., (He et al., 1996) developed a quantitative framework for treating nucleation kinetics and the impact of inhibitors on induction times. According to their formulation, the induction time with inhibitors is given by a nucleation inhibition index (NII):

$$NII = \log\left(\frac{t_{ind}}{t_o}\right) = bC_{inh} \quad (6)$$

Where t_{ind} and t_o are respectively the induction time with and without inhibitor and C_{inh} is the concentration of the inhibitor.

The induction times in equation 6 without inhibitor (t_o) and b are empirically fitted from experimental data such that:

$$\log(t_o) = a1 + \frac{a2}{SI} + \frac{a3}{T} \quad (7)$$

and

$$\log(b) = b1 + b2 * SI + \frac{b3}{T} \quad (8)$$

Substituting equations 7 and 8 into equation 6 and solving for t_{ind} gives:

$$t_{ind} = 10^{(a_1 + \frac{a_2}{SI} + \frac{a_3}{T})} * 10^{\left(10^{b_1 + b_2 * SI + \frac{b_3}{T}}\right) * C_{inh}} \quad (9)$$

Equation 9 is a general equation for the induction time as a function of SI, T, and inhibitor concentration. This formulation has been adopted in multiple investigations of the impact of inhibitors on nucleation kinetics and was found to accurately describe induction times for the major scale forming minerals under a wide range of conditions (Dai et al., 2021; He et al., 1999, 1996; Zhao et al., 2021).

It should be pointed out that while many studies found equation 9 provides great agreement with experimental data, it predicts that in the absence of an inhibitor (i.e., $C_{inh} = 0$), the induction time is reduced to a non-zero constant as SI goes to infinity.

With their limitations described above, both CNT and empirical modeling schemes work well for determining nucleation kinetics, providing insights into nucleation processes, and predicting induction times under a wide range of conditions. In the following, we explore an adaptation of the model to account for dynamic SI conditions.

4.4.2 A proposed model for t_{ind} under a regime of dynamic oversaturation

To adjust the existing models for dynamic conditions one needs to account for SI changing with time. The SI values at induction are similar over the entire range of mass exchange (kw) tested in this study and appear to only significantly change by the concentration of inhibitor (i.e., the metastability zone is insensitive to the rate of SI increase but is influenced by the presence of an inhibitor). Consequently, replacing SI (or Ω) in the static models with a time dependent SI function would not allow for describing the system. Rather, one needs a functional form that enables accounting for different induction times at a similar SI value for a given temperature and inhibitor concentration. One possible solution to this conundrum is to model the induction time with two terms, one term for the rate of nucleation as the function of the environmental conditions (e.g., the static model) and an additional term accounting for the rate in which the SI is changing. Under such a scheme, a functional form for modeling the induction time under a changing SI is given by:

$$t_{ind,dynamic} = f(\Delta SI) * f(t_{ind,static}) \quad (10)$$

where $f(t_{ind,static})$ are one of the common static models (i.e., equations 5 or 9) and $f(\Delta SI)$ is a function that accounts for the rate of increasing SI. In the current study, SI is increased by injection of Ca^{2+} and HCO_3^- ions and the rate of increase depends on the rate of mass transfer. For such a process, $f(\Delta SI)$ will take on the form:

$$t_{ind,dynamic} = \frac{k}{kw} * f(t_{ind,static}) \quad (11)$$

Where k is a kinetic proportionality constant, and k_w is the mass transfer coefficient. Substituting equation 9 into equation 11 gives the following model for t_{ind} :

$$t_{ind} = \frac{k}{k_w} * 10^{\left(a_1 + \frac{a_2}{SI} + \frac{a_3}{T}\right)} * 10^{\left(10^{b_1 + b_2 * SI + \frac{b_3}{T}}\right) * C_{inh}} \quad (12)$$

We used a minimization scheme between the measured and predicted induction times for the 50 °C and 90 °C experiments to derive the coefficients for the model. We then tested the model's predictions against the 70 °C experiments. Figure 5 shows a comparison between the measured and calculated induction times and table 2 summarize the coefficients that provide the best fit between the experimental data and the model predictions.

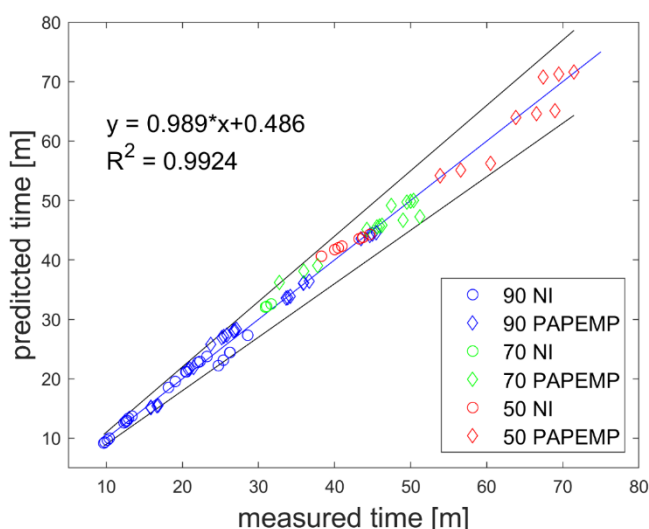


Figure 5: Measured Vs. modeled induction time. NI – no inhibitor, PAPEMP – concentrations of 0.25, 0.5, or 0.7 ppm inhibitor. The error envelope shows $\pm 10\%$ from the measured value.

The difference between the measured induction times and the model predictions compares with the uncertainty reported for experimental measurements of induction times. This excellent agreement between the experiments and model indicate that the suggested modeling scheme adequately describes induction times under varying SI as occurs during energy production and other industrial processes (e.g., RO desalination).

Table 2. Model coefficients		
	Equation 12	Equation 13
k	350	982
a1	-2.51	-19.15
a2	-0.456	-5.81
a3	555.173	10679.0
b1	-3.292	-1.35
b2	-0.003	-0.003
b3	832	740

While equation 12 accounts for the time variation in SI, it still suffers from the limitation discussed above where at infinite SI the induction time does not reduce to zero. To address this issue, we suggest using a power series over SI and T. In addition, the inhibitor term of the equation (e.g., the b dependent term) can be adjusted to eliminate the somewhat unconventional $10^{10(b \dots) * C_{inh}}$ part of the formula. Our proposed model is given by:

$$t_{ind} = \frac{k}{kw} * \left(\frac{a1}{SI * T} + \frac{a2}{SI^2 * T} + \frac{a3}{SI * T^2} \right) * e^{((b1 + b2 * SI + \frac{b3}{T}) * C_{inh})} \quad (13)$$

As before, the model was fitted with the 50 °C and 90 °C data sets and the 70 °C dataset was only used for verification. Figure 6 shows the model predictions VS. the measured observations. Overall, this model provides a good fit ($R^2 = 0.969$). 86% of the predictions are within 10% from the measured data points and all predictions are within 20%. It should be noted that for all experimental conditions where a prediction exceeds 10%, other data points are below that range. This is a result of the variation of the measured induction times. Equation 13 thus provides an overall model for predicting induction times under increasing SI and that satisfies the conditions that: when SI is infinitely large or small, t_{ind} would be infinitely the opposite.

As demonstrated here, it is possible to model induction times under increasing SI and simultaneously treat the nucleation kinetics and polymorphism. Such a scheme is a step forward toward modeling nucleation in natural and engineered environments where SI increases with time.

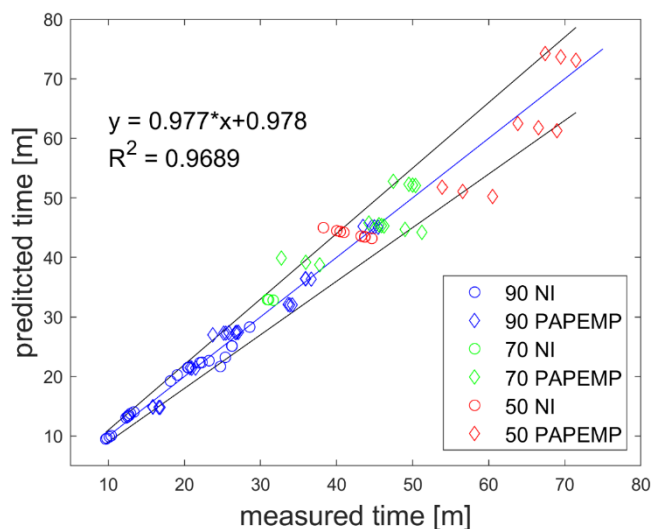


Figure 6. Measured VS. modeled induction times. NI – no inhibitor, PAPEMP – concentrations of 0.25, 0.5, or 0.7 ppm inhibitor. Equation 13 was used for modeling the data. Black lines represent $\pm 10\%$ from the measured values. Note that for every condition where a prediction exceeds 10%, other calculated induction times fall below this value.

4.4.3 Implications and prospective

Scale and its detrimental impact on production is costly. The inhibitors used to prevent scale during energy production from hydrocarbon and hydrothermal reservoirs, and that are added during desalination are not cheap. More importantly, halting production during energy extraction for advanced scale prevention treatments (e.g., scale inhibitor squeeze) or to treat formed scale has a significant monetary cost. In addition, scale inhibitors have a potentially high environmental cost and some of the common inhibitors are forbidden for use by countries with advanced environmental regulation (Mady et al., 2018). Improving models for predicting scale formation can provide a better estimation of scaling risk and the development of prevention procedures that would help mitigate the economic and environmental costs associated with this phenomenon. The good fit between the experimental measurements and the models presented in the previous section demonstrates that the modeling scheme proposed here provides a framework for mathematically describing nucleation kinetics of scale-forming minerals under increasing SI. However, one should consider that both the $f(t_{ind,static})$ and the $f(\Delta SI)$ term might need adjustments to account for varying chemical and physical properties of the fluids for which scale control is necessary.

The ratio between the lattice-building cation and anion of a mineral in solution has a considerable effect on precipitation kinetics (Bracco et al., 2012; Peters et al., 2024; Ruiz-Agudo et al., 2011) and crystal habit (Bracco et al., 2012; Mbogoro et al., 2017; Reiss et al., 2019). This effect causes a wide variation in induction times for a given mineral under similar SI, temperature, salinity, etc. Consequently, models of nucleation kinetics using both the CNT (equation 5) and the empirical scheme (equation 6) discussed above had to address this by adjusting the models to account for this (Dai et al., 2021; Peters et al., 2024). In addition, the

speciation of the active functional groups on the inhibitor between fully dissociated and fully protonated are pH dependent. As a consequence, the retarding efficiency of inhibitors changes with pH (He et al., 1994). As the goal of this study was to explore the feasibility of modeling nucleation time under dynamic conditions, our focus was on varying SI with time and we conducted experiments under constant $\text{Ca}^{2+}/\text{HCO}_3^-$ and pH and the $f(t_{\text{ind},\text{static}})$ term in our model (equation 13) does not explicitly address changes in these parameters.

In addition, during industrial activities where scale control is key for maintaining production the $f(\Delta SI)$ term might be influenced by one or a combination of several processes. These include changes in pressure, pH, temperature (will simultaneously increase and decrease SI for different minerals), salinity, etc. Consequently, the $f(\Delta SI)$ term should be adjusted for different production scenarios. The experimental system described here (section 2.2) allows for an experimental determination of many of the conditions that can affect $f(t_{\text{ind},\text{static}})$, $f(\Delta SI)$, or both. The GC oven framework enables conducting experiments under a variety of both decreasing or increasing temperature gradients. The inflow of cationic, anionic, or both fluids can be adjusted to produce different $\text{Ca}^{2+}/\text{HCO}_3^-$ ratios, applying pH gradients, and different salinities that can be held constant or vary during an experiment. Quantifying the effect of pH, $\text{Ca}^{2+}/\text{HCO}_3^-$, and temperature gradients, and incorporating these into the model is a goal of future research. In addition, we are currently exploring the impact of the dynamic conditions on the nucleation kinetics and metastability zone of the major sulfate-scale-forming minerals.

5. Summary

In this work, we present an experimental system for simultaneously quantifying the nucleation kinetics and determining crystal habit and polymorph as SI increases, as happens during energy production, desalination, and other industrial systems. With this system, we studied the precipitation of CaCO_3 at pH ~ 6.75, I = 1m, 50-90 °C, PAPEMP concentrations of 0-0.7 ppm, and varying rates of increasing SI. We show that: 1. The metastability zone of calcite is independent of the rate at which SI increases; 2. The metastability zone is increased by inhibitor; 3. PAPEMP inhibits calcite nucleation at below ppm concentrations; and 4. PAPEMP has a temperature-dependent effect on the forming CaCO_3 polymorph. Based on our data, we developed a simple algorithm for determining induction time from laser measurements and a numerical model that provides an excellent fit between the experimental and predicted induction times over the entire range of temperatures, SI rate of increase, and concentration of PAPEMP.

CReditT authorship:

Amit G Reiss: Conceptualization, Methodology, Investigation, Analysis, Verification, Writing – original manuscript; Xin Wang: Investigation; Yuqing Ye: Administration, Resources; Amy T Kan: Administration, Resources; Mason B Tomson: Supervision, Funding, Verification, Writing – Review and editing

Declaration of competing interest

The authors declare no competing interest

Acknowledgments

The authors wish to thank Daniel Neuman from Rice University for invaluable technical assistance. This research was funded by members of the Rice University Brine Chemistry Consortium: Aegis, Bachman, Baker Hughes, Chemstream, Chevron, CNPC USA, ConocoPhillips, Equinor, Halliburton, Hess, Imperative Chemicals, Italmatch, Liberty Frac, Occidental Oil and Gas, ONGC, Petrobras, Pioneer Natural Resources, Saudi Aramco, SLB, Shell, SNF, TOTAL.

Notes

The authors declare no competing interests.

Appendix A. A simple algorithm for determining the induction time from a laser measurement

A flow chart representation of the simple algorithm for determining the induction time from the measured laser intensity is shown in figure A1.

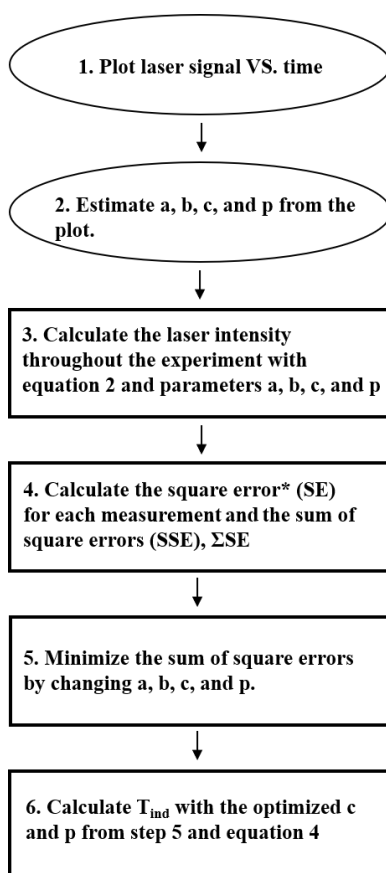


Figure A1. Flow chart describing a simple algorithm for determining induction time from laser intensity. * The square errors (SE) is given by (measured intensity – calculated intensity)².

Bibliography

- Bracco, J.N., Grantham, M.C., Stack, A.G., 2012. Calcite Growth Rates As a Function of Aqueous Calcium-to-Carbonate Ratio, Saturation Index, and Inhibitor Concentration: Insight into the Mechanism of Reaction and Poisoning by Strontium. *Crystal Growth & Design* 12, 3540–3548. <https://doi.org/10.1021/cg300350k>
- Curcio, E., Ji, X., Di Profio, G., Sulaiman, A.O., Fontananova, E., Drioli, E., 2010. Membrane distillation operated at high seawater concentration factors: Role of the membrane on CaCO₃ scaling in presence of humic acid. *Journal of Membrane Science* 346, 263–269. <https://doi.org/10.1016/j.memsci.2009.09.044>
- Dai, C., Dai, Z., Zhao, Y., Wang, X., Paudyal, S., Ko, S., Kan, A.T., Tomson, M.B., 2021. Prediction Models of Barite Crystallization and Inhibition Kinetics: Applications for Oil and Gas Industry. *Sustainability* 13, 8533. <https://doi.org/10.3390/su13158533>
- Dai, Z., Kan, A.T., Shi, W., Zhang, N., Yan, F., Bhandari, N., Zhang, Z., Liu, Y., Ruan, G., Tomson, M.B., 2017. Solubility Measurements and Predictions of Gypsum, Anhydrite, and Calcite Over Wide Ranges of Temperature, Pressure, and Ionic Strength with Mixed Electrolytes. *Rock Mechanics and Rock Engineering* 50, 327–339.
- Dai, Z., Ouyang, B., Wang, X., Li, W., Dai, C., Zhao, Y., Ko, S., Paudyal, S., Kan, A., Tomson, M., 2022a. From water analysis to scale and corrosion control improvements: A Permian Basin example. *Chemical Geology* 610, 121077. <https://doi.org/10.1016/j.chemgeo.2022.121077>
- Dai, Z., Zhang, F., Kan, A.T., Ruan, G., Yan, F., Bhandari, N., Zhang, Z., Liu, Y., Lu, A.Y.-T., Deng, G., Tomson, M.B., 2019. Two-Stage Model Reveals Barite Crystallization Kinetics from Solution Turbidity. *Ind. Eng. Chem. Res.* 58, 10864–10874. <https://doi.org/10.1021/acs.iecr.9b01707>
- Dai, Z., Zhao, Y., Paudyal, S., Wang, X., Dai, C., Ko, S., Li, W., Kan, A.T., Tomson, M.B., 2022b. Gypsum scale formation and inhibition kinetics with implications in membrane system. *Water Research* 225, 119166. <https://doi.org/10.1016/j.watres.2022.119166>
- Didymus, J.M., Oliver, P., Mann, S., DeVries, A.L., Hauschka, P.V., Westbroek, P., 1993. Influence of low-molecular-weight and macromolecular organic additives on the morphology of calcium carbonate. *Faraday Trans.* 89, 2891. <https://doi.org/10.1039/ft9938902891>
- Duroudier, J.-P., 2016. Crystallization and crystallizers, Industrial equipment for chemical engineering set. ISTE Press, London.
- Gill, J.S., 1999. A novel inhibitor for scale control in water desalination. *Desalination* 124, 43–50. [https://doi.org/10.1016/S0011-9164\(99\)00087-9](https://doi.org/10.1016/S0011-9164(99)00087-9)
- Gopi, S., Subramanian, V.K., Palanisamy, K., 2013. Aragonite–calcite–vaterite: A temperature influenced sequential polymorphic transformation of CaCO₃ in the presence of DTPA. *Materials Research Bulletin* 48, 1906–1912. <https://doi.org/10.1016/j.materresbull.2013.01.048>
- Gopi, S.P., Subramanian, V.K., 2012. Polymorphism in CaCO₃ — Effect of temperature under the influence of EDTA (di sodium salt). *Desalination* 297, 38–47. <https://doi.org/10.1016/j.desal.2012.04.015>

- Hasson, D., Drak, A., Semiat, R., 2003. Induction times induced in an RO system by antiscalants delaying CaSO₄ precipitation. *Desalination* 157, 193–207. [https://doi.org/10.1016/S0011-9164\(03\)00399-0](https://doi.org/10.1016/S0011-9164(03)00399-0)
- He, S., Kan, A.T., Tomson, M.B., 1999. Inhibition of calcium carbonate precipitation in NaCl brines from 25 to 90°C. *Applied Geochemistry* 14, 17–25. [https://doi.org/10.1016/S0883-2927\(98\)00033-X](https://doi.org/10.1016/S0883-2927(98)00033-X)
- He, S., Kan, A.T., Tomson, M.B., 1996. Mathematical Inhibitor Model for Barium Sulfate Scale Control. *Langmuir* 12, 1901–1905. <https://doi.org/10.1021/la950876x>
- He, S., Oddo, J.E., Tomson, M.B., 1994. The inhibition of gypsum and barite nucleation in NaCl brines at temperatures from 25 to 90°C. *Applied Geochemistry* 9, 561–567. [https://doi.org/10.1016/0883-2927\(94\)90018-3](https://doi.org/10.1016/0883-2927(94)90018-3)
- Kamal, M.S., Hussein, I., Mahmoud, M., Sultan, A.S., Saad, M.A.S., 2018. Oilfield scale formation and chemical removal: A review. *Journal of Petroleum Science and Engineering* 171, 127–139. <https://doi.org/10.1016/j.petrol.2018.07.037>
- Mady, M.F., Charoensumran, P., Ajiro, H., Kelland, M.A., 2018. Synthesis and Characterization of Modified Aliphatic Polycarbonates as Environmentally Friendly Oilfield Scale Inhibitors. *Energy Fuels* 32, 6746–6755. <https://doi.org/10.1021/acs.energyfuels.8b01168>
- Mbogoro, M.M., Peruffo, M., Adobes-Vidal, M., Field, E.L., O’Connell, M.A., Unwin, P.R., 2017. Quantitative 3D Visualization of the Growth of Individual Gypsum Microcrystals: Effect of Ca²⁺:SO₄²⁻ Ratio on Kinetics and Crystal Morphology. *J. Phys. Chem. C* 121, 12726–12734. <https://doi.org/10.1021/acs.jpcc.7b01566>
- Navarathna, C., Leschied, C., Wang, X., Reiss, A., Ye, Y., Pimentel, D., Shen, Y.-Y., Yao, X., Kan, A., Tomson, M., 2023. A Novel Experiment Setup to Model the Effects of Temperature on Halite Scaling and Inhibition, in: Day 2 Thu, June 29, 2023. Presented at the SPE International Conference on Oilfield Chemistry, SPE, The Woodlands, Texas, USA, p. D021S009R003. <https://doi.org/10.2118/213849-MS>
- Nicoleau, L., Van Driessche, A.E.S., Kellermeier, M., 2019. A kinetic analysis of the role of polymers in mineral nucleation. The example of gypsum. *Cement and Concrete Research* 124, 105837. <https://doi.org/10.1016/j.cemconres.2019.105837>
- Nývlt, J., 1968. Kinetics of nucleation in solutions. *Journal of Crystal Growth* 3–4, 377–383. [https://doi.org/10.1016/0022-0248\(68\)90179-6](https://doi.org/10.1016/0022-0248(68)90179-6)
- Peters, V.F.D., Baken, A., Seepma, S.Y.M.H., Koskamp, J.A., Fernández-Martínez, A., Van Driessche, A.E.S., Wolthers, M., 2024. Effect of Solution Stoichiometry on BaSO₄ Crystallization from Turbidity Measurements and Modeling. *Ind. Eng. Chem. Res.* 63, 78–88. <https://doi.org/10.1021/acs.iecr.3c03612>
- Prieto, M., Putnis, A., Fernández-Díaz, L., López-Andrés, S., 1994. Metastability in diffusing-reacting systems. *Journal of Crystal Growth* 142, 225–235. [https://doi.org/10.1016/0022-0248\(94\)90291-7](https://doi.org/10.1016/0022-0248(94)90291-7)
- Rabizadeh, T., 2023. Investigating the potential of hydroxyethylamino-di(methylene phosphonic acid) in inhibiting gypsum crystallization. *CrystEngComm* 25, 935–944. <https://doi.org/10.1039/D2CE01156E>
- Regenspurg, S., Feldbusch, E., Byrne, J., Deon, F., Driba, D.L., Henniges, J., Kappler, A., Naumann, R., Reinsch, T., Schubert, C., 2015. Mineral precipitation during production of geothermal fluid from a Permian Rotliegend reservoir. *Geothermics* 54, 122–135. <https://doi.org/10.1016/j.geothermics.2015.01.003>

- Reiss, A.G., Ganor, J., Gavrieli, I., 2019. Size Distribution and Morphology of Gypsum Crystals Precipitating from Hypersaline Solutions. *Crystal Growth & Design* 19, 6954–6962. <https://doi.org/10.1021/acs.cgd.9b00735>
- Reiss, A.G., Gavrieli, I., Ganor, J., 2020. The effect of phosphonate-based antiscalant on gypsum precipitation kinetics and habit in hyper-saline solutions: An experimental and modeling approach to the planned Red Sea – Dead Sea Project. *Desalination* 496, 114638. <https://doi.org/10.1016/j.desal.2020.114638>
- Reiss, A.G., Gavrieli, I., Rosenberg, Y.O., Reznik, I.J., Luttge, A., Emmanuel, S., Ganor, J., 2021. Gypsum Precipitation under Saline Conditions: Thermodynamics, Kinetics, Morphology, and Size Distribution. *Minerals* 11, 141. <https://doi.org/10.3390/min11020141>
- Rendel, P.M., Gavrieli, I., Wolff-Boenisch, D., Ganor, J., 2018. Towards establishing a combined rate law of nucleation and crystal growth – The case study of gypsum precipitation. *Journal of Crystal Growth* 485, 28–40. <https://doi.org/10.1016/j.jcrysgro.2017.12.037>
- Reznik, I.J., Ganor, J., Gruber, C., Gavrieli, I., 2012. Towards the establishment of a general rate law for gypsum nucleation. *Geochimica et Cosmochimica Acta* 85, 75–87. <https://doi.org/10.1016/j.gca.2012.02.002>
- Rodriguez-Blanco, J.D., Shaw, S., Benning, L.G., 2011. The kinetics and mechanisms of amorphous calcium carbonate (ACC) crystallization to calcite, viavaterite. *Nanoscale* 3, 265–271. <https://doi.org/10.1039/C0NR00589D>
- Rosenberg, Y.O., Sade, Z., Ganor, J., 2018. The precipitation of gypsum, celestine, and barite and coprecipitation of radium during seawater evaporation. *Geochimica et Cosmochimica Acta* 233, 50–65. <https://doi.org/10.1016/j.gca.2018.04.019>
- Ruiz-Agudo, E., Putnis, C.V., Wang, L., Putnis, A., 2011. Specific effects of background electrolytes on the kinetics of step propagation during calcite growth. *Geochimica et Cosmochimica Acta* 75, 3803–3814. <https://doi.org/10.1016/j.gca.2011.04.012>
- Sanjiv Raj, K., Nirmala Devi, M., Palanisamy, K., Subramanian, V.K., 2021. Individual and synergetic effect of EDTA and NTA on polymorphism and morphology of CaCO₃ crystallization process in presence of barium. *Journal of Solid State Chemistry* 302, 122026. <https://doi.org/10.1016/j.jssc.2021.122026>
- Smeets, P.J.M., Finney, A.R., Habraken, W.J.E.M., Nudelman, F., Friedrich, H., Laven, J., De Yoreo, J.J., Rodger, P.M., Sommerdijk, N.A.J.M., 2017. A classical view on nonclassical nucleation. *Proc. Natl. Acad. Sci. U.S.A.* 114. <https://doi.org/10.1073/pnas.1700342114>
- Tang, Y., Yang, W., Yin, X., Liu, Y., Yin, P., Wang, J., 2008. Investigation of CaCO₃ scale inhibition by PAA, ATMP and PAPEMP. *Desalination* 228, 55–60. <https://doi.org/10.1016/j.desal.2007.08.006>
- Utami, W.S., HERDIANITA, N.R., ATMAJA, R.W., 2014. The Effect of Temperature and pH on the Formation of Silica Scaling of Dieng Geothermal Field, Central Java, Indonesia. Presented at the thirty-Ninth Workshop on Geothermal Reservoir Engineering, Stanford University, Stanford, California.
- Van Der Leeden, M.C., Kashchiev, D., Van Rosmalen, G.M., 1993. Effect of additives on nucleation rate, crystal growth rate and induction time in precipitation. *Journal of Crystal Growth* 130, 221–232. [https://doi.org/10.1016/0022-0248\(93\)90855-Q](https://doi.org/10.1016/0022-0248(93)90855-Q)

718 Van Driessche, A.E.S., Kellermeier, M., Benning, L.G., Gebauer, D. (Eds.), 2017. New
 719 Perspectives on Mineral Nucleation and Growth. Springer International Publishing,
 720 Cham. <https://doi.org/10.1007/978-3-319-45669-0>
 721 Vasina, L.G., Boglovsky, A.V., Koldajeva, I.L., Noev, N.V., 1996. Water-chemical regimes of
 722 distillation plants operating beyond the calcium sulfate dehydrate scale threshold.
 723 Desalination 105, 159–163. [https://doi.org/10.1016/0011-9164\(96\)00070-7](https://doi.org/10.1016/0011-9164(96)00070-7)
 724 Wang, T., Cölfen, H., Antonietti, M., 2005. Nonclassical Crystallization: Mesocrystals and
 725 Morphology Change of CaCO₃ Crystals in the Presence of a Polyelectrolyte Additive. J.
 726 Am. Chem. Soc. 127, 3246–3247. <https://doi.org/10.1021/ja045331g>
 727 Weber, E., Weiss, I.M., Cölfen, H., Kellermeier, M., 2016. Recombinant perlucin derivatives
 728 influence the nucleation of calcium carbonate. CrystEngComm 18, 8439–8444.
 729 <https://doi.org/10.1039/C6CE01878E>
 730 Westin, K.-J., Rasmuson, Å.C., 2005. Nucleation of calcium carbonate in presence of citric acid,
 731 DTPA, EDTA and pyromellitic acid. Journal of Colloid and Interface Science 282, 370–
 732 379. <https://doi.org/10.1016/j.jcis.2004.09.071>
 733 Zhao, Y., Dai, Z., Dai, C., Paudyal, S., Wang, X., Ko, S., Kan, A.T., Tomson, M., 2021.
 734 Semiempirical Model for Predicting Celestite Scale Formation and Inhibition in Oilfield
 735 Conditions. Energy Fuels 35, 11285–11294.
 736 <https://doi.org/10.1021/acs.energyfuels.1c01375>
 737